

# Characterization and on-orbit performance of the Advanced Camera For Surveys CCDs.

Marco Sirianni<sup>a</sup>, Mark Clampin<sup>b</sup>, George F. Hartig<sup>b</sup>, Holland C. Ford<sup>a</sup>, Garth D. Illingworth<sup>c</sup>, Vic Argabright<sup>d</sup>, Bill Burmester<sup>d</sup>, Guido De Marchi<sup>b</sup>, William Koldewyn<sup>d</sup>, Andre' R. Martel<sup>a</sup>, Max Mutchler<sup>b</sup>, Adam Riess<sup>b</sup>, Ronald J. Schrein<sup>d</sup>, and Pamela C. Sullivan<sup>e</sup>

<sup>a</sup> Johns Hopkins University, Baltimore, MD 21218

<sup>b</sup> Space Telescope Science Institute, Baltimore, MD 21218

<sup>c</sup> Univ of California Obs/Lick Observatory, Santa Cruz CA 95064

<sup>d</sup> Ball Aerospace and Technology Corp., Boulder, CO 80301

<sup>e</sup> NASA Goddard Space Flight Center, Greenbelt, MD 20771

## ABSTRACT

We present an overview of the Advanced Camera for Surveys (ACS) CCD detectors performance based on the ground testing and the calibration observations taken during the first four months of ACS operation. ACS has been installed into the Hubble Space Telescope in March 2002 and consists of three different cameras. Two of them employ CCD detectors: the Wide Field Camera a mosaic of two 4096 x 2048 CCDs and the High Resolution Camera a single 1024 x 1024 chip. A review of the on-orbit performance is presented here and also comparison is made with the instrument specifications, published performance expectation and ground test results.

Keywords: HST, ACS, CCDs, WFC, HRC

## 1. INTRODUCTION

The Advanced Camera for Surveys (ACS) is a third generation instrument for the Hubble Space Telescope (HST). ACS has been successfully installed on board of the HST during the last servicing mission in March 2002. ACS has three cameras. The first, the Wide Field Camera, is a high throughput (48% at 660 nm, including the HST optical telescope assembly), wide field (202"x 202"), optical and I-band camera that is half critically sampled at 500 nm. The second, the High Resolution Camera (HRC), is critically sampled at 500 nm, and has a 26" x 29" field of view and 28% throughput at 630 nm. The third camera is a far ultraviolet, Solar-Blind Camera (SBC) that has a relatively high throughput (4.9% at 126 nm) over a 31" x 35" field of view. Ford et al. (1996)<sup>1</sup> described in detail the design of the instruments and of its elements. Two of the three cameras, the WFC and the HRC employ CCD detectors<sup>2,3</sup>. The SBC employs a photon-counting MAMA detector whose performance is described in detail by Tran et al (2002)<sup>4</sup>.

Ford et al 2002<sup>5</sup> (and reference therein) present an overview of the on-orbit performance of the camera. In this paper we will focus on the performance of the CCD detector from an analysis of data obtained from the service mission observatory verification (SMOV) and the first two months of science activity. We will compare the on-flight results with pre-launch calibration data.

## 2. WFC DETECTORS

### 2.1 DESCRIPTION

The focal plane of the WFC consists of two butted 2048x4096 pixel CCDs. The original requirement for these detectors, high quantum efficiency in the visible and near IR, low readout noise and low dark current were met by a commercial design manufactured by Scientific Imaging Technologies (SITE). However, since the CCDs in previous HST instruments showed a rapid degradation in charge transfer efficiency (CTE) in the spacecraft environment, the configuration of the commercial device ST008A has been specifically modified for ACS. The modified design has the serial register along the 4096 pixels edge, to reduce the number of parallel shift to 2048 instead of 4096. After this design modification the chip is buttable along one edge to make 4096x4096 mosaics.

The serial register is split into two halves to allow horizontal split-frame readout through the two amplifiers that terminate the serial register. Although the 2-amps readout will be the default configuration, the entire chip can also be read through a single amplifier, thus increasing the readout time. There are 24 additional extended pixels (physical overscan) on each side of the serial readout register, just before each amplifier. The WFC data will also contain a virtual overscan, 20 rows on top of the chip, obtained over-clocking after the readout of the last CCD row.

The WFC focal plane packages has been described by Clampin et al (1998)<sup>2</sup>. The cosmetic of the WFC flight CCDs has been discussed in Sirianni et al (2002)<sup>3</sup>.

Imaging Area Format	2x 4096 x 2048
Inter-chip gap	~ 50 pixels
Pixel Size	15 $\mu\text{m}$ x 15 $\mu\text{m}$
Serial Register (in each device)	1
Amplifier (in each device)	2
Mini-Channel	3 $\mu\text{m}$ , parallel and serial register
Backside processing:	SITe VIS-AR coating
Clocking	3-phase Multi-Pinned Phase (MPP)
Operating temperature	- 76 C (1 4-stages TEC + 4 2-stages TEC)
Full Well Capacity	~ 76,000 e- (MPP)

**Table 1:** ACS/WFC CCDs specifications.

### 2.2 QUANTUM EFFICIENCY

The WFC CCDs are three phases thinned back-illuminated devices. The backside passivation process and antireflection coating have been performed by SITe with a VIS-AR coating that optimize the response in the I band. The two chips have a very similar response and achieve a mean peak of ~ 74% at 600 nm and ~ 60% at 800 nm. These devices show also a good sensitivity in the blue, but the overall performance of the camera at wavelength lower than 400 nm are limited by the silver coated optics cut-off at ~ 370 nm. Figure 1 shows the measured quantum efficiency curves for the two devices on the focal plane of WFC. Clampin et al. (2002)<sup>6</sup> published the on-orbit total sensitivity of the camera obtained observing few standard stars. The overall sensitivity of the camera is higher than expected from ground measurements (+10-15 % in the visible and +15-20% in the blue). It is likely that part of the enhancement could be due to underestimated detector efficiency.

The CCDs are bonded to a soda glass die which is in turn bonded with indium solder to an aluminum nitride CCD carrier. The flight devices also incorporate a thin aluminum layer over the CCD's frontside gate structure. This

correction to the original design of the CCD architecture has been implemented after the discovery of a scattered light halos in point source images and long slit spectral images at long wavelength ( $> 750$  nm) (Sirianni et al 1998)<sup>7</sup>. The thin metal layer prevents long wavelength light entering in the CCD to be scattered by the impurities in the soda glass die by reflecting the incoming photons straight back in to the CCD. The overall performance is largely improved at wavelengths longer than 750 nm where the layer is effective at suppressing the IR halo. However a residual asymmetrical diffraction-like effect along the CCD serial readout direction is produced at wavelength longer than 800 nm (Hartig et al 2002)<sup>8</sup>. This is probably due to scatter from the CCD channel stop structure or from the front-side clock lines.

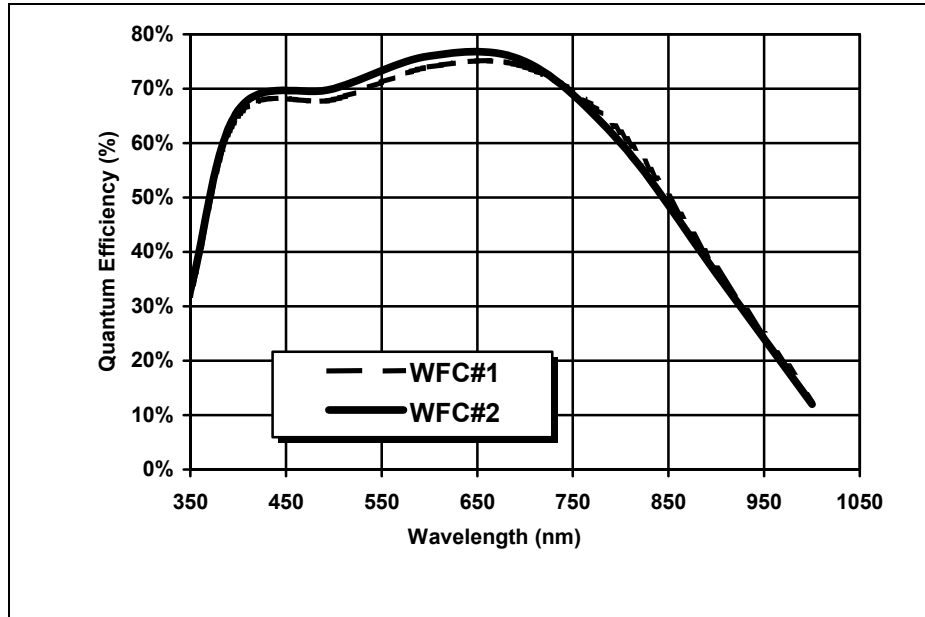


Figure 1: Measured quantum efficiency for the WFC CCDs

### 2.3 BIAS AND READOUT NOISE

Bias reference frames are acquired daily for scientific calibration purpose and monitoring the detectors performance. Every week multiple bias frames are combined together to remove the cosmic rays accumulated during the readout time and to enhance the signal to noise ratio of the bias pattern. In this section we will discuss exclusively the analysis of the bias and read noise for the default four amplifier readout configuration at gain setting  $\sim 1$  e<sup>-</sup>/DN. All the basic CCD parameters are generally consistent with those measured during ground calibration and do not show any significant trend with time.

#### Bias level determination

As described in section 2.1 each quadrant of the WFC focal plane (A & B for WFC-1 and C & D for WFC-2) has two overscan regions: a 24-pixel wide leading physical overscan at columns 1-24 and a 20 rows wide virtual overscan at rows 2049-2068. For bias frames there are therefore three possible measurements of the bias level. All four amplifiers produce a horizontal ramp in the leading overscan which extends up to 18 columns toward the active area<sup>9</sup>. The amplitude of the ramp is different for each amplifier but it is generally larger in the A/D quadrants than in the B/C quadrants. The perturbation associated with the ramp fades gradually and disappears approximately within 15 columns. The bias level from the physical overscan can be safely measured using the last 6 columns adjacent to the active area.

There is no difference between the bias level measured in the virtual overscan and in the active area. However for amplifiers A, B and C the active area has a bias level higher than the physical overscan. The offset varies from amplifier to amplifier and can be as large as 3.5 DN. The cause of this offset is unknown.

### Time evolution of the bias level

Using the bias frames taken during SMOV activities and the first month of science operation, the stability of the bias level in the leading serial overscan region has been studied during the time interval March 2002 – July 2002. The results are shown in figure 2. In general all four quadrants show a similar behavior. During the first hours of activities, after the CCDs had reached their specified operating temperature of  $-76^{\circ}\text{C}$ , the bias level decreased by 25-30 DN from the value measured in the first bias frame acquired during the aliveness test. In the following days and weeks the bias levels has been fairly stable with small variations. Each month the TECs are turned off to allow the CCDs to warm up to  $\sim 19^{\circ}\text{C}$  and anneal hot pixels created by the radiation damage (see section 3.4). After the annealing period (from 10 to 16 hours) the focal plane is brought back to its nominal temperature and bias frames are acquired.

As in the case of the bias frames acquired during day 1, the first image shows a bias level higher than the last frame taken just before the annealing, and only after few hours the bias level settles down to the original level. This effect is clearly visible in figure 2 where the annealing epochs are marked with a vertical dotted line. This behavior is not a concern for calibration purpose because the leading overscan and the active area show the same trend. If we do not consider this monthly feature the bias level for all four WFC quadrants turns out to slowly decrease with time by about 0.02 – 0.03 DN per day. Finally, in addition to the monthly feature AMP B shows an intrinsic scatter of about 20 DN (peak to peak) at any given time in the bias level. Such behavior was already known from ground testing and does not represent a concern because the bias level in the overscan areas changes accordingly with the same amplitude.

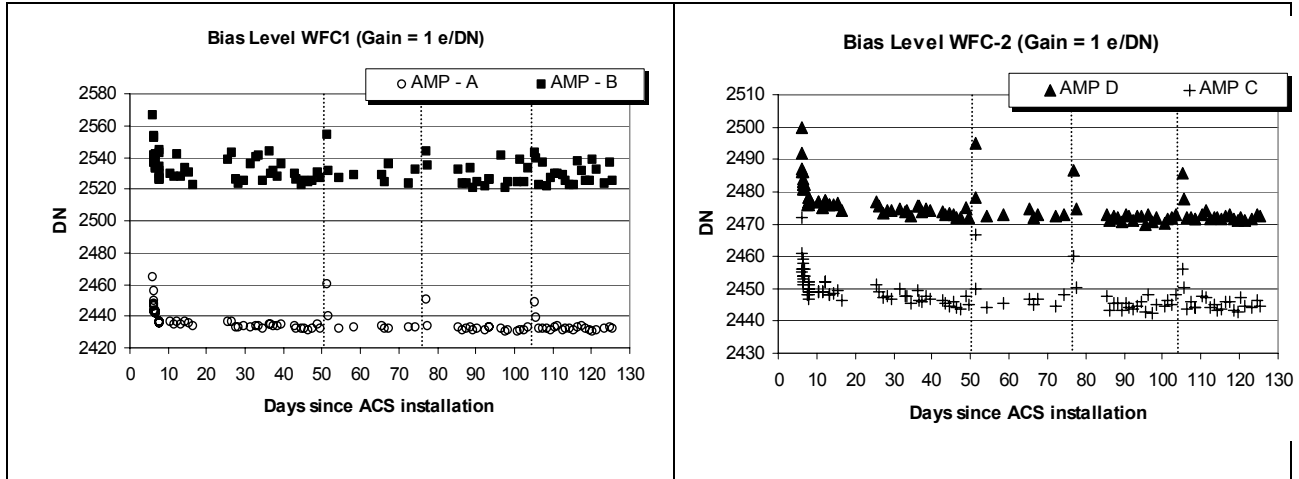


**Figure 2:** Overscan level vs. time for the two WFC CCDs. The dotted vertical lines mark the annealing epochs.

### Time evolution of the read noise

In each quadrant the read noise in the active area and virtual overscan area are in perfect agreement, whereas in the leading physical overscan is between 0.3 and 0.4 lower. Figure 3 shows the time dependence of the read noise measured in the active area of all four quadrants. After a short stabilization period in the first day of activity, the read noise is very stable and does not show any significant variation with time.

The preflight and on-orbit rms read noise of the two WFC CCDs are listed in Table 2. The preflight and on-orbit values are equal within their respective uncertainties and demonstrate the excellent on-orbit isolation from external noise sources in the HST.

CCD	Amplifier	Gain (e-/DN)	RMS Read Noise (e-)	
			Preflight	Flight
WFC - 1	A	1	<b>4.8 ± 0.1</b>	<b>4.99 ± 0.05</b>
		2	5.3 ± 0.1	5.33 ± 0.03
		4	6.1 ± 0.1	6.18 ± 0.10
		8	8.8 ± 0.1	8.90 ± 0.03
	B	1	<b>4.7 ± 0.1</b>	<b>4.89 ± 0.07</b>
		2	5.1 ± 0.1	4.99 ± 0.02
		4	6.0 ± 0.1	5.97 ± 0.08
		8	8.8 ± 0.1	8.74 ± 0.12
WFC - 2	C	1	<b>5.2 ± 0.1</b>	<b>5.16 ± 0.05</b>
		2	5.4 ± 0.1	5.51 ± 0.03
		4	6.2 ± 0.1	6.52 ± 0.17
		8	9.2 ± 0.1	9.35 ± 0.02
	D	1	<b>4.7 ± 0.1</b>	<b>4.82 ± 0.07</b>
		2	5.1 ± 0.1	5.26 ± 0.02
		4	6.2 ± 0.1	6.32 ± 0.03
		8	9.3 ± 0.1	9.22 ± 0.04

**Table 2:** Preflight and on-orbit WFC RMS Read Noise

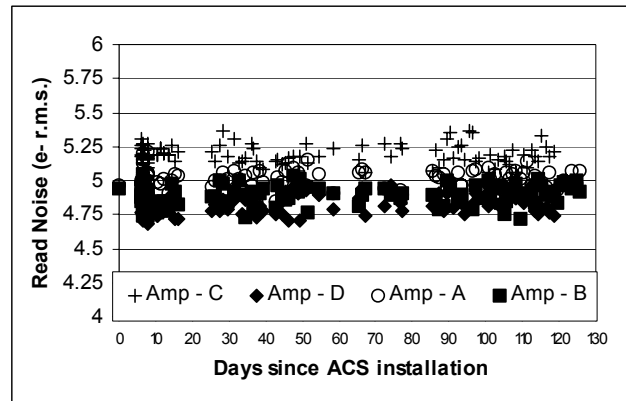


**Figure 3:** WFC rms Read Noise vs time

#### 2.4 DARK CURRENT and HOT PIXEL POPULATION.

The on-orbit dark current and hot pixel population monitoring is carried out daily with 4x1000 sec dark frames. As part of the STScI calibration pipeline, daily “superdark” frames are created after cosmic-ray rejection and median combination of the four frames. We measured the dark rate in different regions along the two CCDs and plotted shows the time evolution of the dark rate in the two chips in Figure 4.

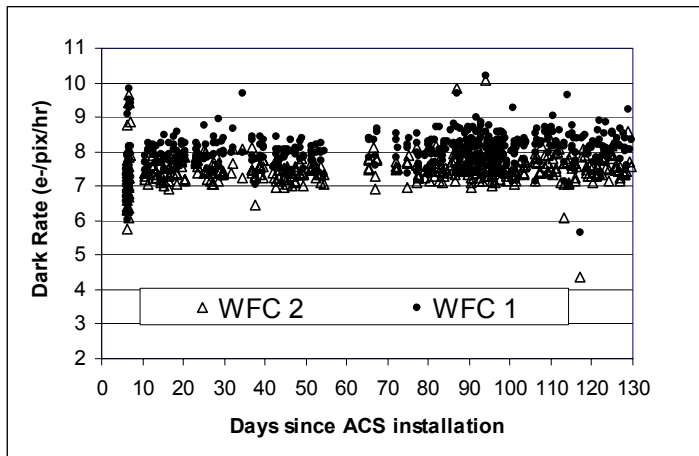


**Figure 4:** WFC Dark rate as a function of time.

We find that, after removing the contribution of hot pixels, the average dark rate is stable at  $8.05 \pm 0.47$  e-/pix/hr for WFC1 and  $7.51 \pm 0.42$  e-/pix/hr for WFC2. The dark frame of WFC2 shows a faint horizontal band along the full length of the chip. The dark rate in the brightest portion of the band exceeds the average rate by  $\sim 2$  e-/pix/hr, in agreement with previous ground measurements.

Like all the CCDs operated in a low earth orbit the ACS CCDs are subject to radiation damage by energetic particles in the radiation belts. Long term radiation damage to the CCDs from high energy protons leads to an increase in dark count rate (mainly from the creation of hot pixels), baseline shifts in the CCD amplifiers, and long term degradation of Charge Transfer Efficiency (CTE). After CTE, one of the major radiation damage mechanisms is the creation of new Si-SiO<sub>2</sub> interface states, which cause increased dark current rates in affected pixels. Riess et al (2002)<sup>10</sup> published an initial study of the hot pixels in the ACS CCDs. They define as “hot” pixels with a dark rate higher than 144 e-/pix/hr, equivalent to 12 times the standard deviation of the Gaussian distribution of the dark current measured just after the launch. With this threshold the daily growth rate is ~ 1200 new hot pixels per day (or ~ 1 every 14000 pixels), comparable to the rate observed for HRC (~ 1 every 12,000 pixels) (see section 3.4). Figure 5 shows the hot pixels daily growth for the WFC detectors.

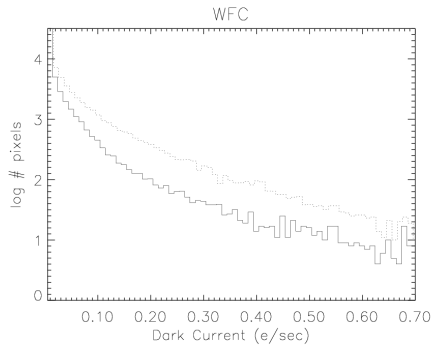


**Figure 5:** Tail of the histogram of dark current in a WFC superdark at two different epochs. All pixels with dark current above 0.04 e-/pix/sec are marked as “hot” and are the product of radiation damage. The number of these pixels can be seen to increase rapidly with time. The full line shows the distribution of dark current for March 15, whereas the dotted line shows the same distribution for March 28.

Like other instrument on HST the ACS CCDs undergo to a monthly annealing process. The TECs are turned off for 10 to 16 hours to allow the CCDs to warm up from  $-76^{\circ}\text{C}$  to  $\sim 19^{\circ}\text{C}$ , a temperature high enough to break the bonds of the radiation damaged lattice and to allow to reconstruct the original structure during cool down. After the annealing period the focal plane is brought back to its nominal temperature and a dark frame is acquired. It is possible to measure the effectiveness of the anneal by comparing two dark frames taken just before and after the annealing process. Figure 6 shows the history of hot pixel growth in the first two month preceding the first two annealing. Only 45%-50% of new hot pixels anneal each month.

As comparison, all the other CCDs on HST (four in Wide Field/Planetary Camera II (WFPC2), one in Space Telescope Imaging Spectrograph (STIS) and also the ACS/HRC CCD) show a better anneal rate ~ 80% for new hot pixels. Subsequent WFC anneals showed the same low effectiveness. The cause for the weakness of the WFC annealing is under investigation. The temperature reached by the two detectors and the length of the anneal are comparable with those of the other instruments. If the anneal rate will remain low in about 3 years ~ 2% of the CCD will be affected by hot pixels, a fraction matching the coverage by cosmic rays in a 1000 second exposure (Riess et al., 2002)

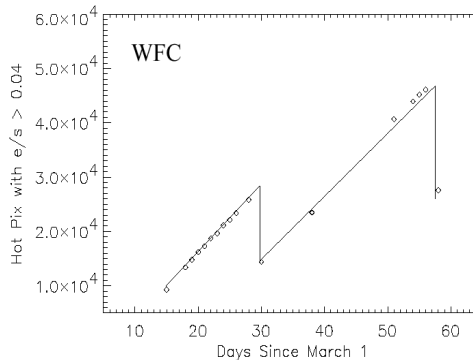


**Figure 6:** Hot pixels trend for the WFC CCDs (Riess et al 2002)<sup>10</sup>

## 2.5 CHARGE TRANSFER EFFICIENCY

Flight data from the instruments on HST that employ CCD detectors (WFPC2 and STIS) show that proton displacement damage has measurably degraded the CTE in those instruments. CTE degradation causes error in stellar photometry,

stellar astrometry and distortion in the observed surface brightness of extended objects (Cawley et al. 2001)<sup>11</sup>. The ACS WFC employs large format CCDs and will be suffering of CTE degradation. The CTE performance of these detectors have been extensively measured on the ground in normal conditions and after they have been radiated with 63 Mev protons to cumulative level that correspond to 1,2.5 and 5 years on orbit (Ford et al. 2002). Several calibration proposals will measure the absolute value of the CTE and monitor its degradation with time. In particular Extended Pixel Edge Response (EPER) and First Pixel Response (FPR) tests have been implemented in the ACS flight software (Jones et al. 1999)<sup>12</sup> and both tests will be repeated 3 times a year covering a large range of signal level. Due to the design of the WFC CCDs EPER measurements will be possible in both the serial and parallel directions, whereas with the FPR test will be only possible to measure the serial CTE. In addition a single monthly measurement at the signal level of 1620 electrons will be repeated for the parallel register to allow a better monitoring of the absolute CTE degradation and to compare the results with ground measurements obtained at the same level with the Fe<sup>55</sup> test. Figure 7 shows the on-orbit parallel CTE for the four quadrants measured one month after the installation on HST. The EPER parallel CTE is very similar for all four detectors and present only marginal departure from ground measurements at the faintest signal levels. The next CTE measurement will indicates if the observed departure is already a sign of initial CTE degradation or is simply due to measurement uncertainties.

Astronomical observation of field of stars will be also used to measure the CTE degradation by comparing the signal measured as a function of the position of the star in the chip. In addition standard calibration frames are used to monitor the relative CTE degradation by measuring the tail of hot pixels and cosmic rays (Riess et al 1999)<sup>13</sup>.

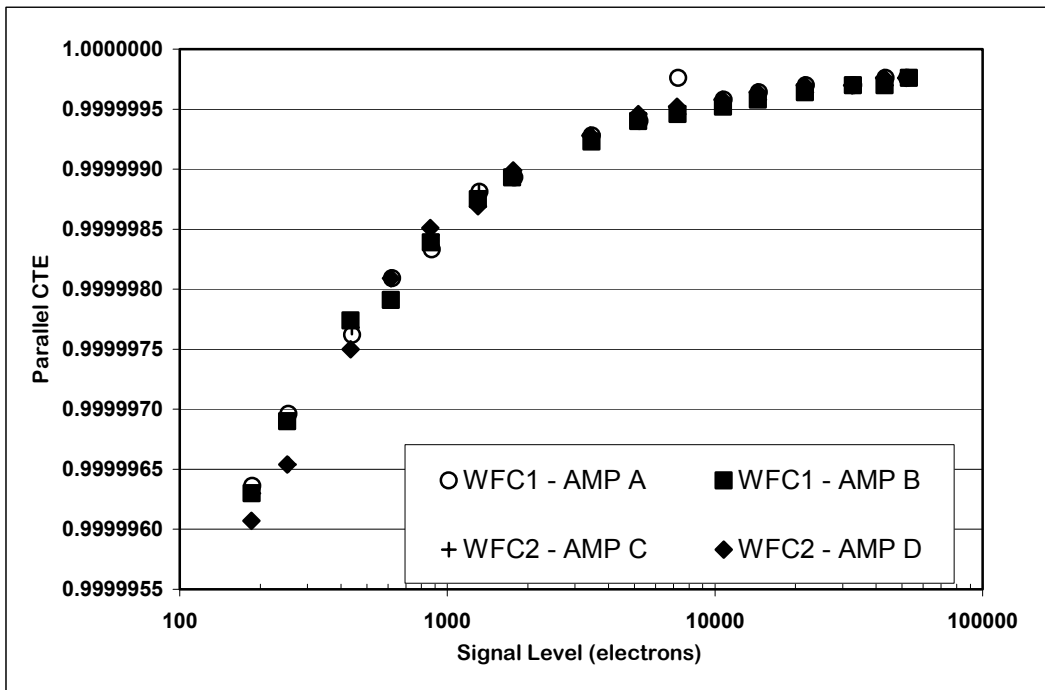


Figure 7: EPER Parallel CTE for the four quadrants of the WFC.

### 3. HRC DETECTORS

#### 3.1 DESCRIPTION

The HRC detector is a single 1024 x 1024 pixel CCD manufactured by SITe. It is based on the backside illuminated STIS 1024x1024 21  $\mu\text{m}$  CCD but it differs in the backside processing that has been optimized for the near UV. This device has four output amplifiers, one at each end of the two serial registers. The array can therefore be divided into 512 x 512 quadrants to maximize the readout time and minimize the CTE loss. The default configuration is a single amplifier readout. There are 19 additional extended pixels (physical overscan) on each side of the serial readout register, just before each amplifier. The HRC data will also contain a virtual overscan, 20 rows on top of the chip, obtained over-clocking after the readout of the last CCD row. The HRC focal plane packages has been described by Clampin et al (1998)<sup>2</sup>. The cosmetic of the HRC flight CCDs has been discussed in Sirianni et al (2002)<sup>3</sup>.

Imaging Area Format	1024 x 1024
Pixel Size	21 $\mu\text{m}$ x 21 $\mu\text{m}$
Serial Register	2
Amplifier	4
Mini-Channel	3 $\mu\text{m}$ , parallel and serial register
Backside processing:	SITe UV AR coating
Clocking	3-phase Multi-Pinned Phase (MPP)
Operating temperature	- 80 C (1 4-stages TEC)
Full well capacity	$\sim$ 150,000 e- (MPP)

**Table 3:** ACS/HRC CCD specifications

#### 3.2 QUANTUM EFFICIENCY

The backside passivation process and antireflection coating have been performed by SITE with a UV coating that produce an elevated response in the visual ( $\sim$  65 % @ 650nm) and near UV ( $\sim$  40% @ 350nm). Figure 8 shows the QE of the device; in the figure no correction for the effects of quantum yield has been applied.

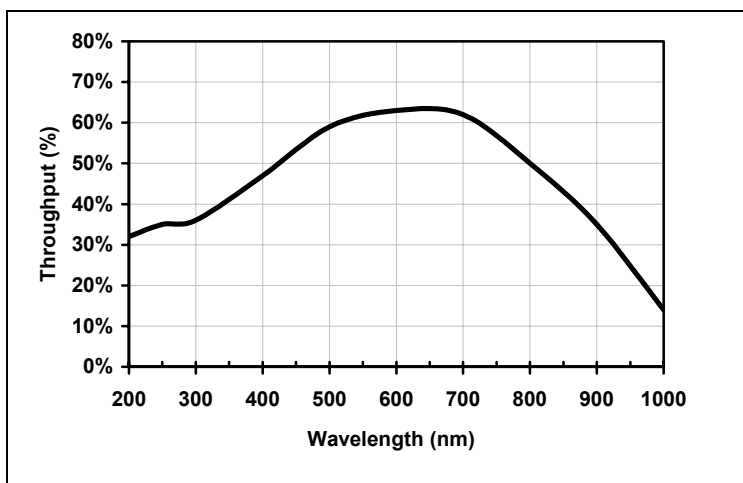


**Figure 8:** Measured quantum efficiency for the HRC CCD.

### 3.3 BIAS AND READOUT NOISE

As for the WFC, bias frames are taken daily for calibration and performance monitoring. The default readout configuration is through the single amplifier C with a nominal gain conversion of 2 e-/DN.

Amplifier	Gain (e-/DN)	RMS Read Noise (e-)	
		Preflight	Flight
A	1	4.41± 0.09	4.74 ± 0.01
	2	4.60± 0.09	4.67 ± 0.04
	4	5.65± 0.09	5.70 ± 0.01
	8	n.a.	n.a.
B	1	4.17± 0.09	4.23 ± 0.01
	2	4.40± 0.09	4.67 ± 0.04
	4	5.40± 0.09	5.70 ± 0.02
	8	n.a.	n.a.
C	1	4.51± 0.09	4.55 ± 0.01
	2	<b>4.74± 0.09</b>	<b>4.71 ± 0.07</b>
	4	4.60± 0.09	4.94 ± 0.15
	8	12.01± 1.00	9.28 ± 0.17
D	1	4.70± 0.09	4.80 ± 0.05
	2	4.98± 0.09	4.90 ± 0.07
	4	5.78± 0.09	6.03 ± 0.02
	8	n.a.	n.a.

**Table 4:** Preflight and on-orbit HRC CCD Read Noise

We investigated the stability of the bias level measured in the active area and overscan regions. In general the virtual overscan and the active area show the same bias level, whereas in the leading physical overscan the bias level is ~ 0.3 DN lower. Figure 9 shows the time dependence of the bias level in DN for the amplifier C. The figure shows all the features already seen in the similar plot for the WFC. Between the very first images taken during the aliveness test and the following days the bias level decreased by ~ 22 DN and has been stable until the first anneal occurred at day 50. The first images after the anneal showed a high bias level which settled down to the normal value within few hours. Subsequent anneals showed a similar trend. The effect is clearly visible in figure 9 where the annealing periods are marked with vertical lines. In the first four months of activity the overall trend shows that the bias level slowly decrease by 0.034 DN per day.

We measured the read noise in the active area and overscan regions for all amplifiers and gain settings. All the three measurements are in agreement within the errors. In table 4 we compare the pre-flight and on-orbit read noise measurements which are in very good agreement. Figure 10 shows the time dependence of the read noise measured in the active area. The read noise is very stable and does not show any significant variation with time.

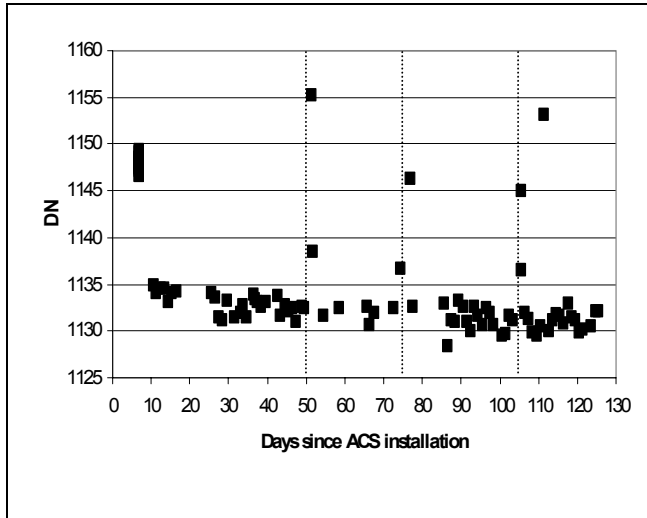


**Figure 9:** HRC bias level as a function of time. The vertical lines mark the annealing epochs.

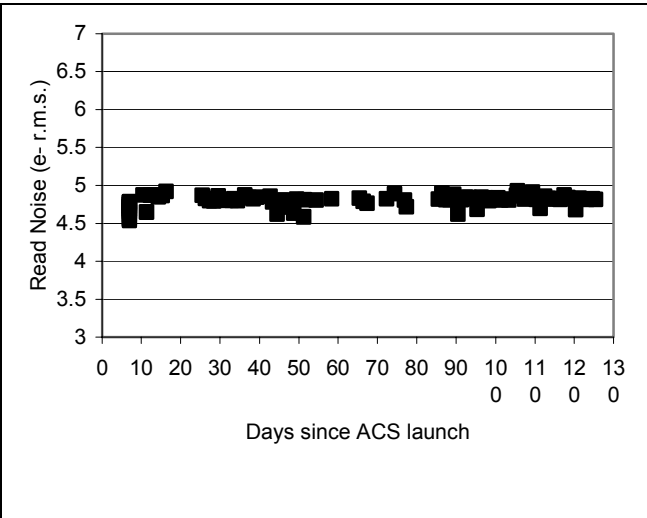


**Figure 10:** HRC rms Read Noise vs time

### 3.4 DARK CURRENT AND HOT PIXEL POPULATION

Dark current and hot pixels population are monitored daily with the acquisition of four-1000 seconds dark frames. We averaged the measured dark rate in different regions of the chip and we find a dark rate of  $9.25 \pm 1.02$  e-/pixel/hr with no significant time dependency (Figure 11). Riess et al. 2002 report a hot pixel growth rate of  $\sim 90$  new hot pixel per day (or  $\sim 1$  every 12,000 pixel) similar to the WFC's rate. One a month the 4-stages TEC is turned off and the detector warm up to  $+22$  C for 10 to 16 hours to fix the damaged lattice structure and anneal the hot pixels. The comparison of the hot pixel population just before and after the annealing period shows that the HRC anneals are quite efficient with  $\sim 80$  % of the new hot pixels fixed (Figure 12). This rate is much better than the one observed in the WFC and it is in agreement with the rate observed for the STIS and the WFPC2 CCDs.

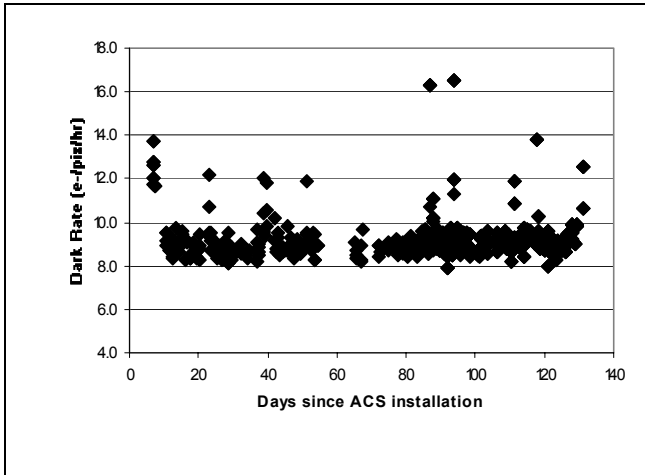


Figure 11: HRC Dark Rate as a function of time

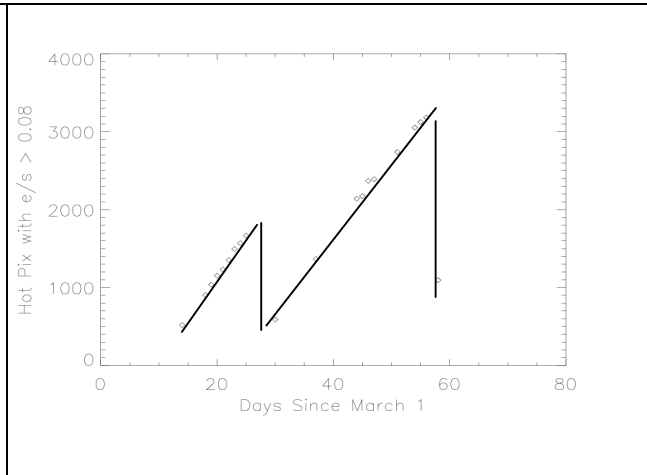


Figure 12: Hot pixel trend for HRC (Riess et al. 2002)

### 3.5 CHARGE TRANSFER EFFICIENCY

The HRC CCD can be readout through all four amplifiers. Therefore both EPER and FPR test can be used for the measurements of the CTE in the parallel and serial direction. All the CTE calibration proposals for the WFC (see section 2.5) are also repeated for the HRC. Figure 13 shows the amplifier C serial and parallel CTE measurement obtained with the FPR test after one month of activity.

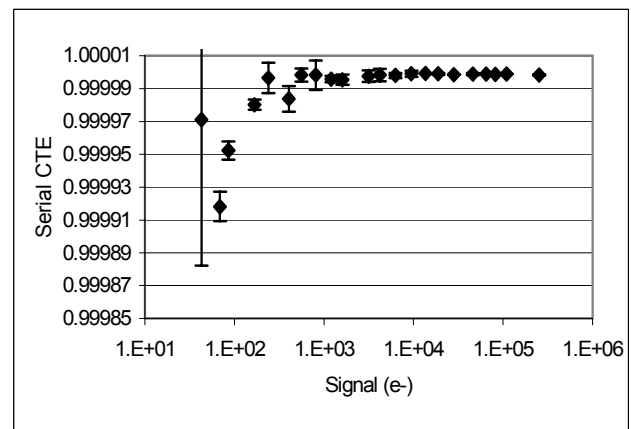
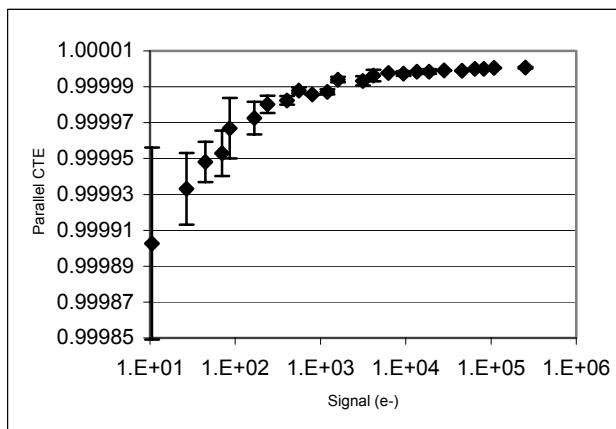


Figure 13: FPR parallel and Serial CTE for the HRC CCD.

## 4. ACKNOWLEDGMENTS

ACS was developed under NASA contract NAS5-32864 and this work was supported by a NASA grant.

## 5. REFERENCES

1. Ford, H.C. and the ACS Science Team, "The HST Advanced Camera for Surveys", in *Space Telescope and Instruments V*, eds. P.Y. Bely & J.B. Breckinridge, SPIE 3356, 234-248, 1998.
2. Clampin, M. and the ACS Science Team, Burmester, B., Blouke, M., and Sirianni, M., "CCD detectors for the HST Advanced Camera for Surveys" in *Space Telescope and Instruments V*, eds. P.Y. Bely & J.B. Breckinridge, SPIE 3356, 332-337, 1998.
3. Sirianni, M., Clampin, M., Hartig, G.F., Ford, H.C., Illingworth, G., Sullivan, P.C., Koldewyn, W., Burmester, B., Schrein, R.J., Albright, V., Lesser, M.P., and Blouke, M.M., "Flight CCD detectors for the Advanced Camera for Surveys" in *Sensors and Camera Systems for Scientific, Industrial and Digital Applications III*, eds. M.M. Blouke, J. Canosa, N. Sampat, SPIE 4669, 202-206, 2002.
4. Tran, H.D., Meurer, G., Ford, H.C., Martel, A.R., Sirianni, M., Bohlin, R., Clampin, M., Cox, C., De Marchi, G., Hartig, G.F., Kimble, R., Argabright, V., "On-Orbit Performance of the ACS Solar Blind Channel" in *Future Visible and UV Space Astrophysics Missions and Instrumentations* eds., J.C. Blades and O.H. Siegmund, SPIE 4854, this volume, 2002.
5. Ford, H.C., Clampin, M., Hartig, G.F., Illingworth, G., Sirianni, M., Martel, A.R., Meurer, G., McCann, W.J., Sullivan, P.C., Bartko, F., Benitez, N., Blakeslee, J., Bouwens, R., Broadhurst, T., Brown, R., Burrows, J.C., Campbell, D., Cheng, E., Feldman, P., Franx, M., Golimowski, D., Gronwall, C., Kimble, R., Lesser, M., Magee, D., Miley, G., Postman, M., Rafal, M., Rosati, P., Sparks, W., Tran, H., Tsvetanov, Z., Volmer, P., White, R., Woodruff, R., "Overview of the Advanced Camera for Surveys On-orbit Performance" in *Future Visible and UV Space Astrophysics Missions and Instrumentations* eds., J.C. Blades and O.H. Siegmund, SPIE 4854, this volume, 2002.
6. Clampin et al. in *Future Visible and UV Space Astrophysics Missions and Instrumentations* eds., J.C. Blades and O.H. Siegmund, SPIE 4854, this volume, 2002.
7. Sirianni, M., Clampin, M., Hartig, G.F., Rafal, M., Ford, H.C., Golimowski, D.A., Illingworth, G., Blouke, M., Lesser, M., Kimble, R., Sullivan, P., Krebs, C. and Yagelowics, J. "Long wavelength scattered light halos in ACS CCDs", in *Optical Astronomical Instrumentation* eds. S. D'Odorico, SPIE 3355, p. 608-612, 1998.
8. Hartig, G.F., Krist, J.E., Martel, A.R., Ford, H.C., Illingworth, G.D., "On-orbit alignment and imaging performance of the HST Advanced Camera for Surveys", in *Future Visible and UV Space Astrophysics Missions and Instrumentations* eds., J.C. Blades and O.H. Siegmund, SPIE 4854, this volume, 2002.
9. Sirianni, M., Martel, A.R., Hartig, G.F., 2001 JHU-ACS internal report, available on line at: [http://acs.pha.jhu.edu/instrument/calibration/results/by\\_item/detector/wfc/build4/overscan/](http://acs.pha.jhu.edu/instrument/calibration/results/by_item/detector/wfc/build4/overscan/)
10. Riess, A., Mutchler, M., Van Orsow, D., 2002 STScI Instrument Science Report ACS 2002-06
11. Cawley L., Goudfloij, P., Whitmore, B., Stiavelli, M., and the CTE working group, 2001, STScI Instrument Science Report WFC3 2001-05.
12. Jones, M.R., Clampin, M., Meurer, G., and Schrein R., 1999, STScI Technical Instrument Report ACS 1999-03.
13. Riess, A., Biretta, J., and Casertano, S., 1999 STScI Instrument Science Report WFPC2 1999-04.